Cell Reports
Physical Science

CellPress
OPEN ACCESS

Article

Critical Current Density as a Performance Indicator for Gas-Evolving Electrochemical Devices

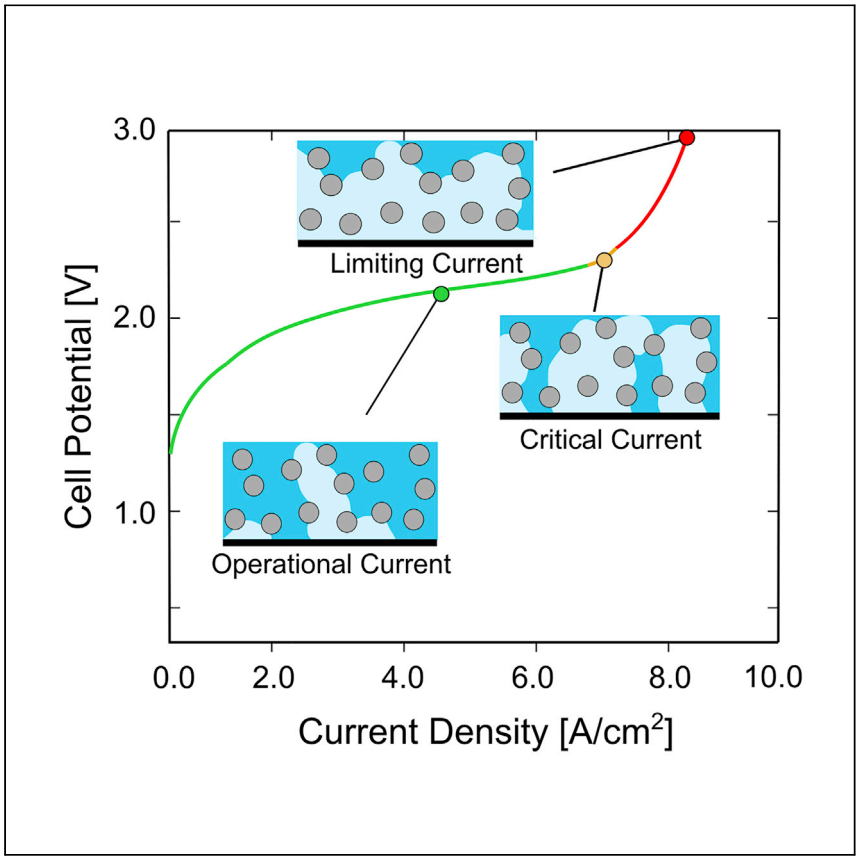

Operating at higher current densities is vital for electrochemical energy conversion devices. In this work, Lee et al. demonstrate the detrimental effects of by-product gas accumulation inside an electrolyzer operating at high current densities. Specifically, the critical current density has been identified as a performance indicator for gas-evolving electrochemical devices.

Jason K. Lee, ChungHyuk Lee, Kieran F. Fahy, ..., David L. Jacobson, Daniel S. Hussey, Aimy Bazylak

abazylak@mie.utoronto.ca

HIGHLIGHTS

The critical current density is a key indicator for electrochemical cell failure

Gas saturation and mass transport losses sharply rise at critical current density

Gas heterogeneously at PTL-CL interface leads to temperature heterogeneity in PTL

High reactant flow rates delay the onset of critical current density

Lee et al., Cell Reports Physical Science 1, 100147
August 26, 2020
https://doi.org/10.1016/j.xcrp.2020.100147

Cell Reports
Physical Science

CellPress
OPEN ACCESS

Article

Critical Current Density as a Performance Indicator for Gas-Evolving Electrochemical Devices

Jason K. Lee,[1] ChungHyuk Lee,[1] Kieran F. Fahy,[1] Benzhong Zhao,[1,2] Jacob M. LaManna,[3] Elias Baltic,[3] David L. Jacobson,[3] Daniel S. Hussey,[3] and Aimy Bazylak[1,4,*]

SUMMARY

Reaching high current densities is absolutely imperative for electrochemical energy conversion, from fuel cells to CO_2 reduction. Here, we identify the existence of a performance indicator for gas-evolving electrochemical energy conversion devices: the critical current density. The critical current density pinpoints a performance inflection point whereby both the gas saturations and mass transport overpotentials suddenly dominate cell performance and exacerbate failure. We elucidate the mass transport behavior of a polymer electrolyte membrane (PEM) water electrolyzer using *in operando* neutron imaging at operating current densities as high as 9 A · cm^{-2}. Product gases become heterogeneously distributed in the porous transport layer adjacent to the catalyst layer and promote disastrous local hotspots. Optimizing new materials and cell architectures with this performance indicator may unlock higher than previously reported performances for electrochemical energy conversion.

INTRODUCTION

The growing rate of carbon dioxide content in the atmosphere is escalating the need for sustainable and renewable energy at an alarming rate. To mitigate the disastrous effects of global warming and hold the global temperature increase below 2 °C by the end of this century,[1] 600 Gt CO_2 must be removed from the atmosphere if we continue to rely on our current energy infrastructure.[2,3] Shifting to carbon-neutral technologies is vital for mitigating global warming, and hydrogen generation via water electrolysis is a promising technology for storing renewable energy to be used for on-demand power when combined with fuel cells. Specifically, polymer electrolyte membrane (PEM) electrolysis can be used to produce high-purity hydrogen (>99.99 vol %) without carbon emissions when coupled with renewable energy sources such as solar and wind.[4,5]

In a PEM electrolyzer, reactant liquid water permeates through the anode porous transport layer (PTL) to the anode catalyst layer (CL), where the oxygen evolution reaction occurs. The resulting protons travel via the membrane, and electrons conduct through an external circuit facilitating the formation of hydrogen via the hydrogen evolution reaction at the cathode catalyst layer. During this process, by-product oxygen gas is generated at the anode and accumulates over the reaction sites and in the pores of the PTL, resulting in undesired system inefficiencies stemming from mass transport losses that contribute up to 25% of the total system losses.[6] These mass transport losses present a disastrous

[1]Thermofluids for Energy and Advanced Material Laboratory, Department of Mechanical and Industrial Engineering, Institute for Sustainable Energy, Faculty of Applied Science and Engineering, University of Toronto, Toronto, ON M5S 3G8, Canada

[2]Department of Civil Engineering, McMaster University, Hamilton, ON L8S 4L7, Canada

[3]Physical Measurement Laboratory, National Institute of Standards and Technology, Gaithersburg, MD, USA

[4]Lead Contact

*Correspondence: abazylak@mie.utoronto.ca

https://doi.org/10.1016/j.xcrp.2020.100147

bottleneck for PEM electrolyzers and prohibit operation at much-coveted high current densities.

Bubbles generated from gas evolution in electrochemical devices significantly influence ohmic, activation, and mass transport losses.[7,8] The examination of mass transport behavior in PEM electrolyzer PTLs is an area of key recent interest.[9–17] Lee et al.[18] simulate the invasion of product gas into liquid water-saturated PTLs, and they calculate the change in liquid water permeability for a range of PTL architectures, including graded porosities. Others[16] suggest that once the PTL exhibits a sufficient porosity:permeability ratio, the effect of permeability on performance becomes negligible. In contrast, PEM electrolyzers experience severe mass transport losses at high current density operations.[6,19] While commercial electrolyzers typically operate at current densities from 1 A · cm^{-2} – 3 A • cm^{-2},[20] current densities up to 15 A • cm^{-2} have been reported by Lewinski et al.[21] However, the mass transport behaviors at high current densities remain spatially unresolved. Although several cases of cell failure are associated with mass transport losses in the literature,[15,22–24] these cell failures are accompanied by low reactant flow rates at low current densities (i < 1.5 A • cm^{-2}). A limiting current has been imaged in the literature, where Panchenko et al.[15] observed an increase in PTL gas saturation at a longitudinal direction at i = 0.6 A • cm^{-2}. However, the transition to mass transport-dominated regime has been overlooked in the field. A further understanding of this transition is necessary to inform strategies for mitigating limiting current density-related issues.

Since the system pressure is closely related to the rate of reactant flow, Zlobinski et al.[25] study the effects of pressure on PEM electrolyzers and demonstrate that the gas accumulation in the PTL does not change with increasing pressure up to 8 bars. Reactant flows within the flow fields also significantly affect mass transport losses in PEM electrolyzers, as is demonstrated in the literature.[26–30] For example, Majasan et al.[27] use optical imaging on a transparent electrolyzer cell to illustrate how mass transport losses in PEM electrolyzers are severely affected by channel flow regime changes (bubbly-to-slug transition). They discuss how the channel flow regime depends on operating temperature, flow rate, and flow field designs. The detailed physics behind mass transport limitations at high current density still remain unknown, and this key understanding of high current density operation is vital for advancing commercial electrochemical energy conversion.

There is a tremendous need to tailor reactant and product flow rates in gas-evolving electrochemical energy conversion from fuel cells to CO_2 reduction, in which optimized flow rates will directly translate into pumping power savings. Since the high capital and operational costs are major bottlenecks to the widespread adoption of clean electrochemical energy conversion, electrolyzer manufacturers must make every effort to curtail those costs. For example, one of the largest commercial electrolyzers available in industry today is from Siemens (Silyzer 300), which is capable of producing 100–2,000 kg hydrogen per hour, while consuming 10 L liquid water per kilogram of hydrogen produced.[20] Commercially deploying electrochemical energy infrastructure during a growing global water crisis demands the efficient use and delivery of liquid water in large-scale systems such as these.

In this work, we report a performance indicator for gas-evolving electrochemical energy conversion. We use *in operando* neutron imaging as a platform to analyze the role of reactant flow rates on the performance of a PEM electrolyzer, and we quantify the fraction of the gas volume to the pore volume in the PTL (referred as the gas saturation), while the reactant flow rate varies from 0.5 mL · min^{-1} , 1.5 mL · min^{-1} , and

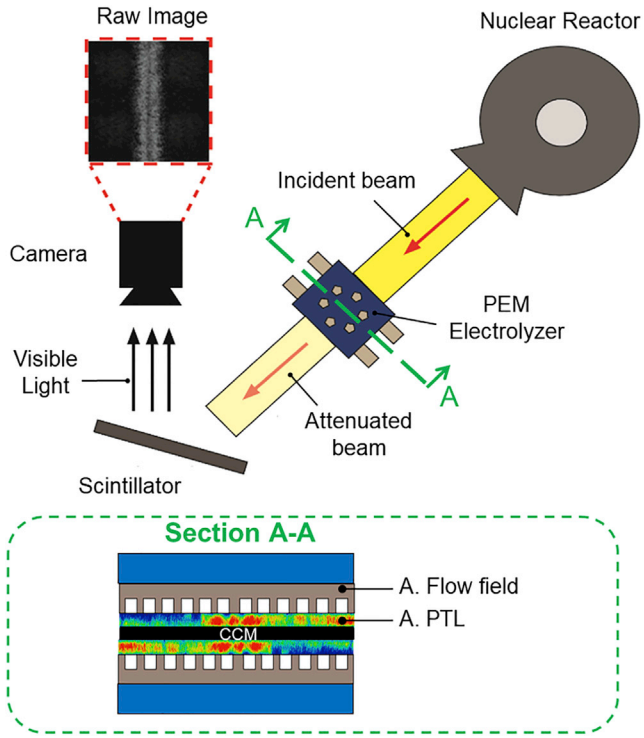

Figure 1. A Schematic of an *In Operando* Neutron Imaging Setup

The neutron beam penetrates at an in-plane direction of the electrolyzer cell. Through image processing of reference and operation images, we quantify the gas saturation at each constant current set point as shown in the subset figure.

3.0 mL • min^{-1} at high current densities (up to 9 A • cm^{-2}). Through concurrent imaging and electrochemical characterization, we correlate PTL gas saturations with mass transport overpotentials. The schematic of the experimental setup is shown in Figure 1.

RESULTS AND DISCUSSION

Electrochemical Performance under Mass Transport-Dominated Regime

We performed electrochemical analysis to study the relationship between mass transport overpotential and low reactant flow rates at high current densities. The polarization curves are collected simultaneously with neutron images to correlate the gas saturation with the performance of an operating PEM electrolyzer. At current densities < 5 A • cm^{-2}, the cell performance exhibits similar cell potentials for all 3 flow rates. However, at current densities > 5 A • cm^{-2}, the cell performance depends strongly on the prescribed flow rate (Figure 2A). Specifically, at the lowest flow rate (0.5 mL • min^{-1}), the mass transport overpotential increases, which leads to immediate cell failure at current densities > 5 A • cm^{-2}. At an intermediate flow rate (1.5 mL • min^{-1}), the cell sustains operation up to i = 7 A • cm^{-2}, but with significant mass transport losses, as illustrated by the exponential increase in the overpotentials shown in the polarization curve (Figure 2A). The mass transport limitations observed at i = 7 A • cm^{-2} are accompanied by a 35 % (0.17 V) increase in η_{MT} compared to the highest flow rate (3.0 mL • min^{-1}) (Figure 2B). At the highest flow rate of 3.0 mL • min^{-1}, the mass transport limitations are not severe until a fairly high current density is reached (i.e., i = 9 A • cm^{-2}). Moreover, we observe increases in cell temperatures up to 0.3°C at higher current densities (i > 5 A • cm^{-2}). This increase in temperature with increasing current density is observed for all flow rates, and the lowest temperature is observed at the highest

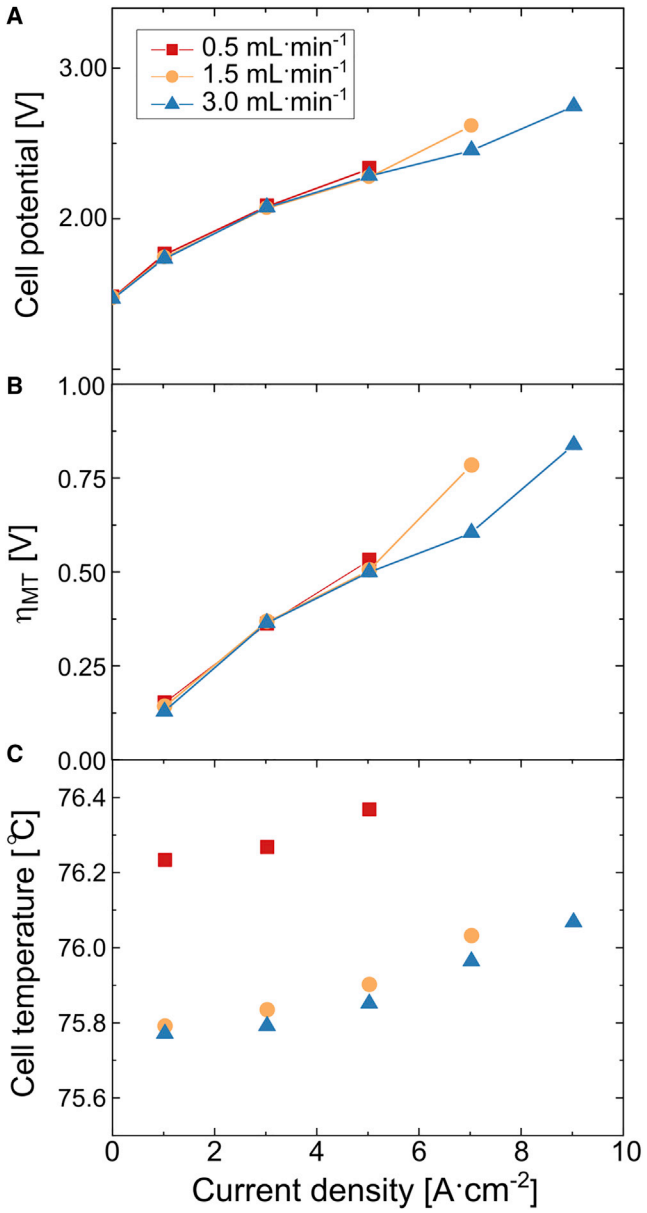

Figure 2. Electrochemical Performance Acquired during *In Operando* Imaging

(A) Galvanostatic polarization curve for flow rates of 0.5 mL · min^{-1} , 1.5 mL · min^{-1} , and 3.0 mL • min^{-1}. Higher cell potential is observed for 1.5 mL • min^{-1} at 7 A • cm^{-2}.

(B) Mass transport overpotential as a function of current density. The mass transport overpotential increases significantly at 7 A • cm^{-2} for 1.5 mL • min^{-1} and at 9 A • cm^{-2} for 3.0 mL • min^{-1}.

(C) The cell temperature as a function of current density. Increases in cell temperature become significant at higher current densities (i > 5 A • cm^{-2}).

flow rate, which is attributed to enhanced water circulation (Figure 2C). We demonstrate in this work that a sufficient reactant flow rate is necessary to minimize mass transport losses and avoid cell failures, especially for higher current density operations.

Extreme Gas Saturation Triggers Critical Current Density

Via *in operando* neutron imaging, we characterize gas saturation in the anode PTL. The gas saturation profile shows the accumulation of generated gas in the in-plane

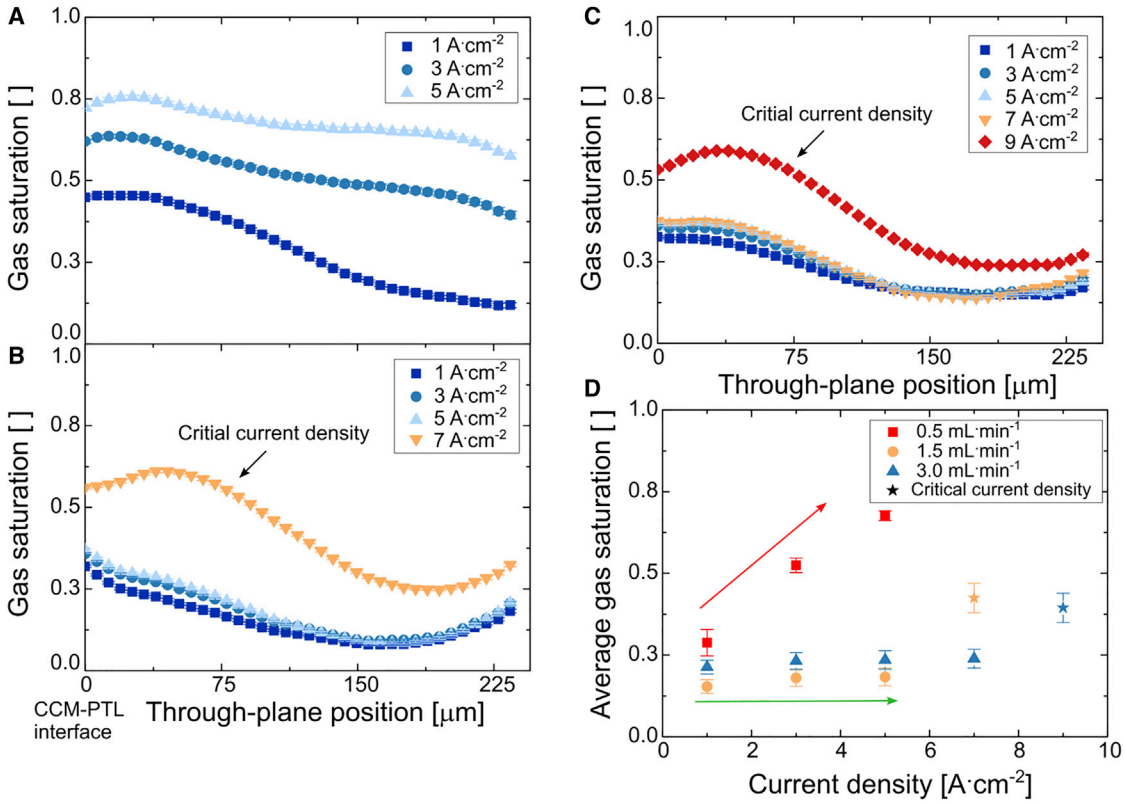

Figure 3. Gas Saturation Profiles for the Anode PTL

(A–C) The flow rates are (A) 0.5 mL • min^{-1}, (B) 1.5 mL • min^{-1}, and (C) 3.0 mL • min^{-1}. The gas saturation profile indicates the amount of gas present at a position over a period of 75 s proceeding the establishment of steady state as a function of the PTL thickness (through-plane distance). The error bars indicate the standard deviation of the average through-plane gas saturation distribution.

(D) The overall average gas saturation as a function of current density under the tested flow rates. The gas saturation increases with increasing current density at a flow rate of 0.5 mL • min^{-1}, but gas saturation remains fairly constant for flow rates > 0.5 mL • min^{-1}. A significant increase in gas saturation is observed at the critical current density. The error bars indicate the standard deviation of the average through-plane gas saturation distribution over the entire PTL.

direction (i.e., axis parallel to the beam) as a function of the through-plane position in the PTL (i.e., PTL thickness). The gas saturation indicates the amount of gas present at a certain through-plane position over a period of 75 s after the establishment of steady-state cell operation (deviation of cell potential < 5% for a period of 5 min). Although the gas behavior is dynamic, the drainage of gas into the liquid water at steady state results in continuous gas transport through the same percolation path, as demonstrated by Lee et al.[31,32]

We use saturation profiles acquired from *in operando* neutron imaging to further demonstrate the need for a sufficient reactant flow rate. The lowest flow rate of 0.5 mL • min^{-1} is inadequate for removing the gas generated in the PTL. This is indicated by an increase in gas saturation with increasing current density (Figure 3A). However, at higher flow rates, the gas saturation in the PTL remains fairly constant with increasing current density. This has been observed in other works featuring gas saturation profiles for PTLs in PEM electrolyzers, such as that by Seweryn et al.[33] Even at a relatively high current density (i = 5 A • cm^{-2}), the gas saturation in the PTL is only 18% at 1.5 mL • min^{-1}. Therefore, we suggest that a sufficient reactant flow rate is required to facilitate gas removal in the PTL. This recommendation is in agreement with previous neutron imaging work by Hoeh

et al.,[34] who observe reduced gas saturation inside the flow channels when a higher reactant flow rate is applied to the electrolyzer. It is important to note that we observe slightly higher gas saturations with 1.5 mL • min^{-1} compared to 3.0 mL • min^{-1} at low current densities. We attribute the slightly higher gas saturation to the lower temperature exhibited at 3.0 mL • min^{-1}; our previous work demonstrates that higher temperatures lead to lower gas saturations.[35] The Reynolds number characterizes the ratio between inertial and viscous forces in the flow channel, and is calculated for the applied flow rates to report normalized flow rates, using the following relation:

$$Re = \frac{\rho v l}{\mu}. \quad \text{(Equation 1)}$$

where ρ is the density of liquid water (kg • m^{-3}), v is the velocity of water in the channel (m • s^{-1}), l is the characteristic length (length of the parallel channel [0.0125 m]), and μ is the dynamic viscosity of water (Pa • s). The Reynolds number indicates the flow regime within the channels, which affects the flow to the PTL (flow direction normal to the channels).[26,30] The Reynolds number is calculated as Re = 70, 209, and 418 for flow rates of 0.5 mL · min^{-1}, 1.5 mL · min^{-1}, and 3.0 mL • min^{-1}, respectively. The reactant water exhibits laminar flow behavior for all flow rates (Re < 2,300). Our work shows for the first time that sufficient flow rates must be applied to effectively remove gas from the PTL when increasing the current density.

Increasing the current density for a fixed flow rate leads to significant increases in the gas saturation inside the anode PTL. Specifically, at the intermediate flow rate of 1.5 mL • min^{-1}, the PTL gas saturation increases from 18% to 42% at 7 A • cm^{-2} (Figure 3B), and at the highest flow rate (3.0 mL • min^{-1}), the gas saturation increases from 24% to 39% at 9 A • cm^{-2} (Figure 3C). Moreover, this significant increase in gas saturation occurs concurrently with the increase in η_{MT} (Figure 2B). This is the first instance of experimentally observing the existence of a critical current density. We report that at the critical current density, the simultaneous increase in PTL gas saturation and η_{MT} is observed. Beyond the critical current density, the rate of gas generation exceeds the rate of gas removal, which hinders the reactant liquid water from reaching the reaction sites. While the gas saturation in the PTL remains fairly constant before reaching the critical current density, the increase in cell temperature is evident with increasing current density (Figure 2C). This relationship between temperature and current density indicates how high flow rates are desired, not only for mitigating the critical current density but also for mitigating the increase in the cell temperature.

While the concept of limiting current density is well established in many electrochemical applications, such as fuel cells and batteries, the concept of critical current density reported here is completely distinct from limiting current density. Limiting current in electrochemical applications refers to the current density at which reactions are completely halted due to the blockage of reactant by-product at the electrode surface. However, critical current density refers to the onset of cell failure. For example, in solid-state batteries the critical current density is used as an indicator for the current density at which dendrite growth becomes severe.[36,37] With this work, we are the first to show that critical current densities exist for membrane-based gas-evolving electrolysis, where extreme gas saturation contributes to increases in mass transport overpotentials, which exacerbates cell failure. Mass transport losses are observed in the literature, such as the work of Lickert et al.,[38] in which the authors observe increases in mass transport losses depending

on operating conditions and PTL microstructure. Within the ranges of the increased mass transport regions observed in these studies, there exists a critical current density in which gas saturation simultaneously increases with mass transport losses. Beyond this critical current density, the electrolyzer cell is susceptible to failure.

Heterogeneous Gas Distribution at Critical Current Density

The reactant flow rate also plays a vital role in gas distribution in the PTL. Several studies from the literature discuss heterogeneous current and temperature distributions observed at near-reactant starvation conditions.[22,23] Specifically, Immerz et al.[22] demonstrate using a segmented electrolyzer cell that mass transport overpotential increases near the outlet region of the cell. In this work, we present for the first time the visualization and quantification of heterogeneous gas distributions due to insufficient reactant flow rates (Figure 4). At 0.5 mL • min^{-1}, the gas saturation in the PTL continuously increases with increasing current density. The majority of the regions in the PTL at flow rate of 0.5 mL • min^{-1} are saturated with gas, especially toward the central region of the active area. For 1.5 mL • min^{-1} and 3.0 mL • min^{-1}, the gas saturation is relatively low at the PTL-flow field interface, and the gas is uniformly distributed near the CL-PTL interface. We expect that gas generated in the catalyst layer is removed through established gas pathways in the PTL regardless of the increases in the local gas pressure, as demonstrated by the micromodel experiments of Lee et al.[31] The result is a minimal change in the gas distribution, with increasing current density before the onset of the critical current density. Furthermore, Hoeh et al.[34] and Lee et al.[39] report increases in gas volume within flow channels with increasing current density, which signifies that gas pathways established at low current densities are sufficient for the removal of gas (even at higher current densities) before reaching the critical current density. However, as soon as the critical current density is reached, we observe that gas becomes heterogeneously distributed near the CL-PTL interface, toward the central region of the active area (Figures 4C and 4D). The positions of the local hotspots are expected to vary based on the flow field and PTL design used in the electrolyzer cell. The increase in gas saturation indicates that the supplied reactant flow rate is inadequate for removing the generated gas at the critical current density. Therefore, increases in the local gas pressure with inadequate reactant flow rates lead to the establishment of additional gas pathways in the PTL (and subsequent increase in gas saturation). The resulting increase in gas saturation and heterogeneous gas distributions contribute to the higher mass transport overpotential observed at critical current densities (Figure 2B). Extreme gas saturation at the CL-PTL interface is potentially a cause for heterogeneous current and temperature distributions observed at near-starvation conditions, as previously reported in the literature.[22,23,40] Specifically, the high gas saturation reduces the effective thermal conductivity (due to displacement of water with gas), and we expect to see an increase in the local temperature of the PTL. The combined effects of the local temperature and gas distribution manifest as the local current distribution in the PEM electrolyzer. Our experiment focuses on a single commercial PTL: a sintered titanium powder-based PTL, which is one of the most widely used PTLs for PEM electrolyzers.[41,42] The authors suggest future studies to examine the impact of additional PTLs and PTL microstructures on the onset of the critical current density, such as bilayer structured PTLs[43] or PTLs with a porosity gradient (low to high from the CL-PTL interface to the flow field interface, respectively),[18,44] which facilitates effective gas removal and hence delays the onset of critical current density.

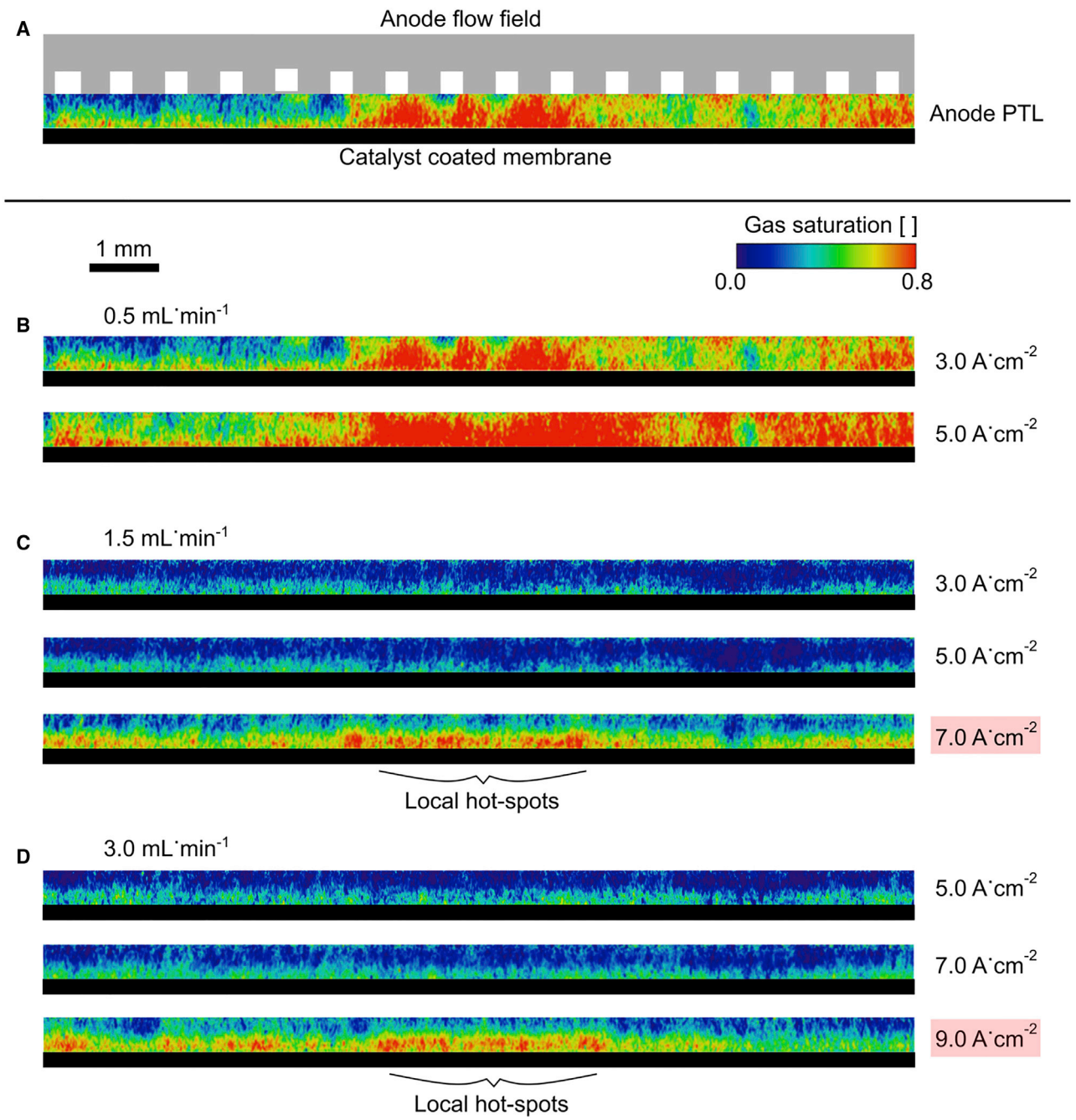

Figure 4. Radiographs of the Anode PTL during Operation

(A) Schematic of the visualized region of the anode compartment. The lower interface is the CL-PTL interface, and the upper interface is the PTL-flow field interface.

(B–D) Gas distribution through the anode PTL for (B) 0.5 mL • min^{-1}, (C) 1.5 mL • min^{-1}, and (D) 3.0 mL • min^{-1}. The gas saturation is relatively low near the PTL-flow field interface with sufficient reactant flow; however, the gas saturation increases and becomes heterogeneously distributed near the CL-PTL interface at the critical current density. The scale bar represents 1 mm.

Here, we report a new performance indicator for gas-evolving electrochemical energy conversion devices, and we elucidate the underlying mass transport behavior of PEM electrolyzers at higher than ever reported current densities measured with

in operando imaging (double the highest reported in the literature[45]). We demonstrate that a sufficient flow rate is required for effective gas removal, thereby minimizing mass transport losses occurring at high current density operations. The gas saturation in the anode PTL, quantified using neutron imaging, demonstrates that gas saturation sharply increases at the critical current density, which is also accompanied by an increase in the mass transport overpotential. At this performance inflection point, the gases become heterogeneously distributed near the CL-PTL interface, creating conditions that are susceptible to degradation from non-uniform current and temperature distributions.[22,23] We recommend the use of PTLs exhibiting effective gas removal, such as the hierarchical structured PTL[43] or novel PTLs with through-pores,[46] to delay the onset of the critical current density of PEM electrolyzers. The PEM electrolyzer system should operate below the critical current density to avoid the undesired degradation caused by local temperature and current density effects. The critical current density must be used as a key performance indicator to design materials and cell architectures that defer the onset of mass transport limitations and thereby enable the highest current densities possible.

EXPERIMENTAL PROCEDURES

Resource Availability

Lead Contact

Information and requests for resources and materials should be directed to the Lead Contact, Aimy Bazylak (abazylak@mie.utoronto.ca).

Materials Availability

Commercially available PTLs and CCMs were purchased from Mott Corporation and Ion Power, respectively.

Data and Code Availability

The imaging data that supports the findings of this study can be made available from the Lead Contact upon request.

General Procedures

The effect of reactant flow rate on the performance of a PEM electrolyzer operating under the mass transport-dominated regime is examined through a combination of electrochemical characterization and neutron imaging. Galvanostatic polarization curves are obtained for a range of flow rates at high current densities (up to 9 A • cm^{-2}). The Tafel approximation is performed to isolate the mass transport overpotentials, and *in operando* neutron imaging is used to correlate oxygen gas saturations to these mass transport overpotentials. We determine the partial gas saturation in the anode PTL, which further describes the mass transport mechanisms at the mass transport-dominated regime.

PEM Electrolyzer Cell

A single PEM electrolyzer cell is used for this study. Grade 2 titanium flow field plates with 16 parallel channels (12.50 mm × 500 μm × 500 μm) are used at the anode and cathode compartments. A commercially available catalyst-coated Nafion HP membrane with an iridium catalyst (1.0 mg • cm^{-2}) at the anode and a platinum catalyst (0.3 mg • cm^{-2}) at the cathode (HYDRion HP, Ion Power) is used as the membrane-electrode assembly, with the active area of the cell being 0.8 cm^2. Sintered titanium powder PTLs with a porosity of 35% and a thickness of 254 μm (1100 Series, Mott Corp.) are used as both anode and cathode PTLs, which are compressed down to 237 μm using polytetrafluoroethylene gaskets.

In Operando PEM Electrolyzer Experiment

The performance at low flow rates and high current densities is evaluated using galvanostatic polarization in conjunction with the Tafel approximation. Polarization curves were repeated for each of the flow rates at 0.5 mL · min^{-1}, 1.5 mL · min^{-1}, and 3.0 mL • min^{-1}. A constant flow rate of deionized water is supplied to both anode and cathode compartments using a commercial peristaltic pump (Masterflex L/S precision variable-speed console drive, Cole-Parmer) in line with a pulse dampener. The temperature of the PEM electrolyzer cell is maintained at 78 °C by circulating heated water through both endplates using a heated water bath (Isotemp 4100R20, Fisher Scientific).

A power supply (Genesys 750W, TDK-Lambda) supplies current during the galvanostatic polarization. Constant current densities are applied from the open circuit to 9 A • cm^{-2} for all operating conditions. Each constant current operation is held for 15 min, and we report values averaged from the last 5 min to ensure fully developed steady-state operation.

Tafel slope analysis is conducted after each polarization curve to approximate the mass transport overpotential at different reactant flow rates. A potentiostat (VersaSTAT 3, AMETEK Scientific Instruments) is used to measure the high-frequency resistance (HFR) and Tafel slope from 40 to 300 mA • cm^{-2}. Each current step is held for 20 s. The mass transport overpotential is calculated using the following equation:

$$\eta_{mass\ transport} = E_{cell} - E_{rev} - \eta_{ohmic} - \eta_{kinetic}\ . \quad \text{(Equation 2)}$$

where $\eta_{mass\ transport}$ is the mass transport overpotential (V), E_{cell} is the measured cell potential (V), $E_{reversible}$ is the reversible potential (V), η_{ohmic} is the ohmic overpotential (V), and $\eta_{kinetic}$ is the kinetic overpotential (V). As discussed in previous literature, η_{ohmic} accounts for the membrane resistance and other electronic resistance.[47,48] The protonic transport resistance in the CL is included in $\eta_{mass\ transport}$. However, we attribute the nonlinear increase in $\eta_{mass\ transport}$ with increasing current density observed in this work to the two-phase induced mass transport losses. We apply an empirical correlation demonstrated by LeRoy et al.[49] to calculate the reversible potential at the operating cell temperature (T):

$$E_{rev} = 1.5184 - 1.5421 \times 10^{-3} \cdot T + 9.523 \times 10^{-5} \cdot T \cdot lnT + 9.84 \times 10^{-8} \cdot T^2. \quad \text{(Equation 3)}$$

We obtain the ohmic overpotential based on the measured HFR and current density:

$$\eta_{ohmic} = i \cdot R_{ohmic}. \quad \text{(Equation 4)}$$

where i is the current density (A • cm^{-2}), and R_{ohmic} is the measured HFR (Ω • cm^2). The HFR used to calculate ohmic overpotential is assumed to be constant over the range of current densities used. An average HFR value measured from 40 to 300 mA • cm^{-2} is used. Since the literature has demonstrated that the HFR slightly decreases with increasing current density at low flow rates, our assumption of constant current density is expected to lead to a somewhat conservative estimate of mass transport overpotential from the Tafel approximation.[22,40] Finally, the kinetic overpotential is calculated using the following relation:

$$\eta_{kinetic} = b \cdot \log_{10}\left(\frac{i}{i_0}\right). \quad \text{(Equation 5)}$$

where b is the Tafel slope (V/dec), and i_0 is the apparent exchange current density (A • cm^{-2}). It is important to note that we assume that kinetic overpotential follows

the Tafel relation throughout the examined current density in our calculation of mass transport overpotential. While the high-volume fraction of gas may affect the electrochemical surface area and kinetic overpotential, we expect that the mass transport loss is the dominant factor at high current densities, as observed in previous works.[23,24]

In Operando Neutron Imaging

In operando neutron imaging enables the quantification of PTL gas saturation at various operating conditions. We use *in operando* neutron imaging at the Neutron Imaging Facility (BT-2) located at the National Institute of Standards and Technology (NIST) Center for Neutron Research (Gaithersburg, MD).[50]

The neutron beam penetrates the electrolyzer cell in an in-plane direction (parallel to the flow channels), and the attenuated beam is converted to visible light using a Gd_2O_2S:Tb scintillator. The visible light is then captured using an Andor Neo scientific complementary metal-oxide semiconductor (sCMOS) detector with an 85-mm lens and a PK13 extension tube, which gives an effective pixel pitch of 15 μm. The exposure time of 25 s was used to ensure a sufficient neutron flux. Before each experiment, the electrolyzer cell is flushed with liquid water for 30 min to remove as much residual gas in the reference image, as revealed from our previous work.[51] A reference image is then taken in the absence of an applied current, and the acquired reference image is used for comparison with the subsequent operational images.

To quantify oxygen gas saturation in the anode PTL, the acquired neutron images are processed via the following procedure:

Median combination of 3 raw images
Median filtering of 3 × 3 pixels
Image registration
Apply modified Beer-Lambert law[50]

The median combination corrects for the random noise caused by the beam characteristics (gamma spots), and the median filtering eliminates noise from electronics (hotspots). The image registration process corrects for the artifact caused by the operating mechanisms of the NIST reactor.[50] Lastly the gas thickness is quantified by using the relation demonstrated by Hussey et al.[50] based on the Beer-Lambert law:

$$t_{gas} = \sqrt{-\frac{\ln(I/I_0)}{\beta_w} + \frac{\Sigma_w^2}{4\beta_w^2}} - \frac{\Sigma_w}{2\beta_w}. \qquad \text{(Equation 6)}$$

where t_{gas} is the gas thickness from each pixel (mm), I is the intensity of the operation images, and I_0 is the intensity of the reference image. Σ_w and β_w are fitting parameters for the beamline, which are 0.38483 mm^{-1} and −0.00947 mm^{-2}, respectively. An average of the last 5 min of the total 15 min of operation is used to calculate the gas thickness to ensure steady state. Figure 5A shows the raw image obtained from *in operando* neutron imaging, and Figure 5B is after the image processing procedures.

ACKNOWLEDGMENTS

This work was supported by the Natural Sciences and Engineering Research Council of Canada (NSERC) Discovery Grants Program and the Canada Research Chairs

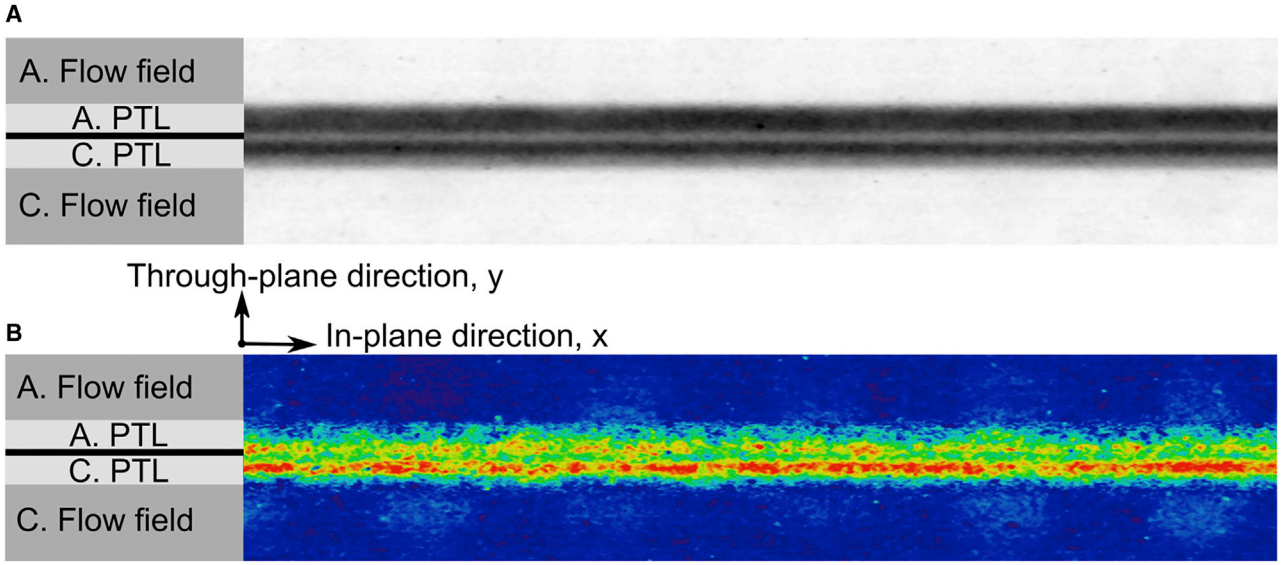

Figure 5. A Schematic of the Image Processing Process Procedure
(A) Raw image obtained from *in operando* neutron imaging.
(B) Processed image after the Beer-Lambert law.

Program. Graduate scholarships awarded to J.K.L. from the NSERC Alexander Graham Bell Canada Graduate Scholarships – Doctoral Program, the Queen Elizabeth II/Edward Rygiel Graduate Scholarship in Science and Technology, the Ontario Graduate Scholarship, and the Glynn Williams Fellowships are also gratefully acknowledged. A portion of this work was supported by the NIST and the NIST Physical Measurement Laboratory. Certain trade names and company products are mentioned in the text or identified in an illustration to adequately specify the experimental procedure and equipment used. In no case does such identification imply recommendation or endorsement by the NIST, nor does it imply that the products are necessarily the best available for the purpose.

AUTHOR CONTRIBUTIONS

J.K.L., Conceptualization, Methodology, Software, Formal Analysis, Investigation, Writing – Original Draft Preparation, Writing – Review & Editing, Visualization, and Project Administration. CH.L., Methodology, Investigation, and Writing – Review & Editing. K.F.F., Investigation and Writing – Review & Editing. B.Z., Investigation and Writing – Review & Editing. J.M.L., Resources and Writing – Review & Editing. E.B., Resources and Writing – Review & Editing. D.L.J., Resources and Writing – Review & Editing. D.S.H., Resources and Writing – Review & Editing. A.B., Supervision, Methodology, Formal Analysis, Funding Acquisition, Resources, and Writing – Review & Editing.

DECLARATION OF INTERESTS

The authors declare no competing interests.

Received: April 13, 2020
Revised: July 1, 2020
Accepted: July 13, 2020
Published: August 19, 2020; corrected online April 14, 2021

REFERENCES

1. Rogelj, J., den Elzen, M., Höhne, N., Fransen, T., Fekete, H., Winkler, H., Schaeffer, R., Sha, F., Riahi, K., and Meinshausen, M. (2016). Paris Agreement climate proposals need a boost to keep warming well below 2 °C. Nature *534*, 631–639.

2. Luderer, G., Vrontisi, Z., Bertram, C., Edelenbosch, O.Y., Pietzcker, R.C., Rogelj, J., De Boer, H.S., Drouet, L., Emmerling, J., and Fricko, O. (2018). Residual fossil CO 2 emissions in 1.5–2 C pathways. Nat. Clim. Chang. *8*, 626–633.

3. Kaya, Y., Yamaguchi, M., and Geden, O. (2019). Towards net zero CO 2 emissions without relying on massive carbon dioxide removal. Sustain. Sci. *14*, 1739–1743.

4. Ursua, A., Gandia, L.M., and Sanchis, P. (2012). Hydrogen Production From Water Electrolysis: Current Status and Future Trends. Proc. IEEE *100*, 410–426.

5. Carmo, M., Fritz, D.L., Mergel, J., and Stolten, D. (2013). A comprehensive review on PEM water electrolysis. Int. J. Hydrogen Energy *38*, 4901–4934.

6. Suermann, M., Schmidt, T.J., and Büchi, F.N. (2015). Investigation of Mass Transport Losses in Polymer Electrolyte Electrolysis Cells. ECS Trans. *69*, 1141–1148.

7. Angulo, A., van der Linde, P., Gardeniers, H., Modestino, M., and Fernández Rivas, D. (2020). Influence of Bubbles on the Energy Conversion Efficiency of Electrochemical Reactors. Joule *4*, 555–579.

8. Lee, C., Zhao, B., Lee, J.K., Fahy, K.F., Krause, K., and Bazylak, A. (2020). Bubble Formation in the Electrolyte Triggers Voltage Instability in CO_2 Electrolyzers. iScience *23*, 101094.

9. Garcia Navarro, J.C., Schulze, M., and Friedrich, K.A. (2018). Understanding the role of water flow and the porous transport layer on the performance of Proton Exchange Membrane Water Electrolyzers. ACS Sustain. Chem. Eng. *7*, 1600–1610.

10. Garcia-Navarro, J., Schulze, M., and Friedrich, K. (2019). Measuring and modeling mass transport losses in proton exchange membrane water electrolyzers using electrochemical impedance spectroscopy. J. Power Sources *431*, 189–204.

11. Kang, Z., Yu, S., Yang, G., Li, Y., Bender, G., Pivovar, B.S., Green, J.B., and Zhang, F. (2019). Performance improvement of proton exchange membrane electrolyzer cells by introducing in-plane transport enhancement layers. Electrochim. Acta *316*, 43–51.

12. Lee, J., and Bazylak, A. (2019). Stochastic Modelling For Controlling the Structure of Sintered Titanium Powder-Based Porous Transport Layers for Polymer Electrolyte Membrane Electrolyzers. J. Electrochem. Soc. *166*, F1000–F1006.

13. Lee, C.H., Banerjee, R., Arbabi, F., Hinebaugh, J., and Bazylak, A. (2016). Porous Transport Layer Related Mass Transport Losses in Polymer Electrolyte Membrane Electrolysis: A Review. In ASME 2016 14th International Conference on Nanochannels, Microchannels, and Minichannels/ASME 2016 Heat Transfer Summer Conference/ASME 2016 Fluids Engineering Division Summer Meeting, American Society of Mechanical Engineers 50343, V001T07A003-V001T07A003.

14. Leonard, E., Shum, A.D., Normile, S., Sabarirajan, D.C., Yared, D.G., Xiao, X., and Zenyuk, I.V. (2018). Operando X-ray tomography and sub-second radiography for characterizing transport in polymer electrolyte membrane electrolyzer. Electrochim. Acta *276*, 424–433.

15. Panchenko, O., Borgardt, E., Zwaygardt, W., Hackemüller, F.J., Bram, M., Kardjilov, N., Arlt, T., Manke, I., Müller, M., Stolten, D., and Lehnert, W. (2018). In-situ two-phase flow investigation of different porous transport layer for a polymer electrolyte membrane (PEM) electrolyzer with neutron spectroscopy. J. Power Sources *390*, 108–115.

16. Schuler, T., Schmidt, T.J., and Büchi, F.N. (2019). Polymer Electrolyte Water Electrolysis: Correlating Performance and Porous Transport Layer Structure: Part II. Electrochemical Performance Analysis. J. Electrochem. Soc. *166*, F555–F565.

17. Schuler, T., De Bruycker, R., Schmidt, T.J., and Büchi, F.N. (2019). Polymer Electrolyte Water Electrolysis: Correlating Porous Transport Layer Structural Properties and Performance: Part I. Tomographic Analysis of Morphology and Topology. J. Electrochem. Soc. *166*, F270–F281.

18. Lee, J., Lee, C., and Bazylak, A. (2019). Pore network modelling to enhance liquid water transport through porous transport layers for polymer electrolyte membrane electrolyzers. J. Power Sources *437*, 226910.

19. Ojong, E.T., Kwan, J.T.H., Nouri-Khorasani, A., Bonakdarpour, A., Wilkinson, D.P., and Smolinka, T. (2017). Development of an experimentally validated semi-empirical fully-coupled performance model of a PEM electrolysis cell with a 3-D structured porous transport layer. Int. J. Hydrogen Energy *42*, 25831–25847.

20. Grigoriev, S., Fateev, V., Bessarabov, D., and Millet, P. (2020). Current status, research trends, and challenges in water electrolysis science and technology. Int. J. Hydrogen Energy. https://doi.org/10.1016/j.ijhydene.2020.03.109.

21. Lewinski, K.A., van der Vliet, D., and Luopa, S.M. (2015). NSTF advances for PEM electrolysis-the effect of alloying on activity of NSTF electrolyzer catalysts and performance of NSTF based PEM electrolyzers. ECS Trans. *69*, 893.

22. Immerz, C., Schweins, M., Trinke, P., Bensmann, B., Paidar, M., Bystroň, T., Bouzek, K., and Hanke-Rauschenbach, R. (2018). Experimental characterization of inhomogeneity in current density and temperature distribution along a single-channel PEM water electrolysis cell. Electrochim. Acta *260*, 582–588.

23. Sun, S., Xiao, Y., Liang, D., Shao, Z., Yu, H., Hou, M., and Yi, B. (2015). Behaviors of a proton exchange membrane electrolyzer under water starvation. RSC Advances *5*, 14506–14513.

24. Li, H., Inada, A., Fujigaya, T., Nakajima, H., Sasaki, K., and Ito, K. (2016). Effects of operating conditions on performance of high-temperature polymer electrolyte water electrolyzer. J. Power Sources *318*, 192–199.

25. Zlobinski, M., Schuler, T., Buchi, F.N., Schmidt, T.J., and Boillat, P. (2020). Transient and steady state two-phase flow in anodic porous transport layer of proton exchange membrane water electrolyzer. J. Electrochem. Soc. *167*, 084509.

26. Ito, H., Maeda, T., Nakano, A., Hasegawa, Y., Yokoi, N., Hwang, C., Ishida, M., Kato, A., and Yoshida, T. (2010). Effect of flow regime of circulating water on a proton exchange membrane electrolyzer. Int. J. Hydrogen Energy *35*, 9550–9560.

27. Majasan, J.O., Cho, J.I., Dedigama, I., Tsaoulidis, D., Shearing, P., and Brett, D.J. (2018). Two-phase flow behaviour and performance of polymer electrolyte membrane electrolysers: electrochemical and optical characterisation. Int. J. Hydrogen Energy *43*, 15659–15672.

28. Majasan, J.O., Cho, J.I., Maier, M., Dedigama, I., Shearing, P.R., and Brett, D.J. (2018). Effect of Anode Flow Channel Depth on the Performance of Polymer Electrolyte Membrane Water Electrolyser. ECS Trans. *85*, 1593–1603.

29. Dedigama, I., Angeli, P., Ayers, K., Robinson, J.B., Shearing, P.R., Tsaoulidis, D., and Brett, D.J. (2014). In situ diagnostic techniques for characterisation of polymer electrolyte membrane water electrolysers - flow visualisation and electrochemical impedance spectroscopy. Int. J. Hydrogen Energy *39*, 4468–4482.

30. Dedigama, I., Angeli, P., van Dijk, N., Millichamp, J., Tsaoulidis, D., Shearing, P.R., and Brett, D.J. (2014). Current density mapping and optical flow visualisation of a polymer electrolyte membrane water electrolyser. J. Power Sources *265*, 97–103.

31. Lee, C., Hinebaugh, J., Banerjee, R., Chevalier, S., Abouatallah, R., Wang, R., and Bazylak, A. (2017). Influence of limiting throat and flow regime on oxygen bubble saturation of polymer electrolyte membrane electrolyzer porous transport layers. Int. J. Hydrogen Energy *42*, 2724–2735.

32. Lee, C., Zhao, B., Abouatallah, R., Wang, R., and Bazylak, A. (2019). Compressible-Gas Invasion into Liquid-Saturated Porous Media: Application to Polymer-Electrolyte-Membrane Electrolyzers. Phys. Rev. Appl. *11*, 054029.

33. Seweryn, J., Biesdorf, J., Schmidt, T.J., and Boillat, P. (2016). Communication—Neutron Radiography of the Water/Gas Distribution in the Porous Layers of an Operating Electrolyser. J. Electrochem. Soc. *163*, F3009–F3011.

34. Hoeh, M.A., Arlt, T., Kardjilov, N., Manke, I., Banhart, J., Fritz, D.L., III, Ehlert, J., Lüke, W., and Lehnert, W. (2015). In-operando neutron radiography studies of polymer electrolyte membrane water electrolyzers. ECS Trans. *69*, 1135.

35. Lee, C., Lee, J., Zhao, B., Fahy, K., LaManna, J., Baltic, E., Hussey, D., Jacobson, D., Schulz, V., and Bazylak, A. (2020). Temperature-dependent gas accumulation in polymer electrolyte membrane electrolyzer porous transport layers. J. Power Sources *446*, 227312.

36. Krauskopf, T., Dippel, R., Hartmann, H., Peppler, K., Mogwitz, B., Richter, F.H., Zeier, W.G., and Janek, J. (2019). Lithium-Metal Growth Kinetics on LLZO Garnet-Type Solid Electrolytes. Joule *3*, 2030–2049.

37. Hatzell, K.B. (2020). Not All Lithium Filaments Are the Same in Solid-State Batteries. Joule *4*, 719–721.

38. Lickert, T., Kiermaier, M.L., Bromberger, K., Ghinaiya, J., Metz, S., Fallisch, A., and Smolinka, T. (2020). On the influence of the anodic porous transport layer on PEM electrolysis performance at high current densities. Int. J. Hydrogen Energy *45*, 6047–6058.

39. Lee, C., Lee, J.K., George, M.G., Fahy, K.F., LaManna, J.M., Baltic, E., Hussey, D.S., Jacobson, D.L., and Bazylak, A. (2020). Reconciling temperature-dependent factors affecting mass transport losses in polymer electrolyte membrane electrolyzers. Energy Convers. Manage. *213*, 112797.

40. Immerz, C., Bensmann, B., Trinke, P., Suermann, M., and Hanke-Rauschenbach, R. (2018). Local Current Density and Electrochemical Impedance Measurements within 50 cm Single-Channel PEM Electrolysis Cell. J. Electrochem. Soc. *165*, F1292–F1299.

41. Millet, P., Mbemba, N., Grigoriev, S.A., Fateev, V.N., Aukauloo, A., and Etiévant, C. (2011). Electrochemical performances of PEM water electrolysis cells and perspectives. Int. J. Hydrogen Energy *36*, 4134–4142.

42. Babic, U., Suermann, M., Büchi, F.N., Gubler, L., and Schmidt, T.J. (2017). Critical Review—Identifying Critical Gaps for Polymer Electrolyte Water Electrolysis Development. J. Electrochem. Soc. *164*, F387–F399.

43. Schuler, T., Ciccone, J.M., Krentscher, B., Marone, F., Peter, C., Schmidt, T.J., and Büchi, F.N. (2019). Hierarchically Structured Porous Transport Layers for Polymer Electrolyte Water Electrolysis. Adv. Energy Mater. *10*, 1903216.

44. Lettenmeier, P., Kolb, S., Zielke, L., Thiele, S., Fallisch, A., Sata, N., Gago, A.S., and Friedrich, K.A. (2017). Comprehensive Investigation of Novel Pore-Graded Gas Diffusion Layers for High-Performance and Cost-Effective Proton Exchange Membrane Electrolyzers. Energy Environ. Sci. *10*, 2521–2533.

45. Minnaar, C., De Beer, F., and Bessarabov, D. (2019). Current density distribution of electrolyzer flow fields: in situ current mapping and neutron radiography. Energy Fuels *34*, 1014–1023.

46. Mo, J., Kang, Z., Retterer, S.T., Cullen, D.A., Toops, T.J., Green, J.B., Jr., Mench, M.M., and Zhang, F.Y. (2016). Discovery of true electrochemical reactions for ultrahigh catalyst mass activity in water splitting. Sci. Adv. *2*, e1600690.

47. Babic, U., Schmidt, T.J., and Gubler, L. (2018). Communication—Contribution of Catalyst Layer Proton Transport Resistance to Voltage Loss in Polymer Electrolyte Water Electrolyzers. J. Electrochem. Soc. *165*, J3016–J3018.

48. Lopata, J., Kang, Z., Young, J., Bender, G., Weidner, J., and Shimpalee, S. (2020). Effects of the Transport/Catalyst Layer Interface and Catalyst Loading on Mass and Charge Transport Phenomena in Polymer Electrolyte Membrane Water Electrolysis Devices. J. Electrochem. Soc. *167*, 064507.

49. LeRoy, R.L., Bowen, C.T., and LeRoy, D.J. (1980). The thermodynamics of aqueous water electrolysis. J. Electrochem. Soc. *127*, 1954–1962.

50. Hussey, D.S., Spernjak, D., Weber, A.Z., Mukundan, R., Fairweather, J., Brosha, E.L., Davey, J., Spendelow, J.S., Jacobson, D.L., and Borup, R.L. (2012). Accurate measurement of the through-plane water content of proton-exchange membranes using neutron radiography. J. Appl. Physiol. *112*, 104906.

51. Lee, C., Lee, J., Zhao, B., Fahy, K., and Bazylak, A. (2020). Transient Gas Distribution in Porous Transport Layers of Polymer Electrolyte Membrane Electrolyzers. J. Electrochem. Soc. *167*, 024508.